Experimental relative entanglement potentials of single-photon states

Josef Kadlec,[1] Karol Bartkiewicz,[2] Antonín Černoch,[3] Karel Lemr,[1] and Adam Miranowicz[2]
[1]*Joint Laboratory of Optics of Palacký University and Institute of Physics AS CR, Faculty of Science, Palacký University in Olomouc, 17. listopadu 12, 771 46 Olomouc, Czech Republic*
[2]*Institute of Spintronics and Quantum Information, Faculty of Physics, Adam Mickiewicz University, 61-614 Poznań, Poland*
[3]*Joint Laboratory of Optics of Palacký University and Institute of Physics AS CR, Institute of Physics of the Academy of Sciences of the Czech Republic, 17. listopadu 50a, 772 07 Olomouc, Czech Republic*

(Received 29 January 2024; revised 10 June 2024; accepted 16 July 2024; published 16 August 2024)

Entanglement potentials (EPs) enable the characterization and quantification of the nonclassicality of single-mode optical fields by measuring the entanglement generated through beam splitting. We experimentally generated single-photon states and tomographically reconstructed the corresponding two-qubit states to determine EPs defined via popular two-qubit measures of entanglement. These include the potentials for the relative entropy of entanglement (REEP), concurrence, and negativity. Among our experimental states, we found those that are very close (at least for some ranges of parameters) to the theoretical upper and lower bounds on relative EPs (or relative nonclassicality), i.e., when one EP is maximized or minimized for a given value of another EP. We experimentally confirmed the counterintuitive theoretical result of Miranowicz *et al.* [Phys. Rev. A **92**, 062314 (2015)] that the relative nonclassicality (specifically, the negativity potential for given values of the REEP) of single-photon states can be increased by dissipation.

DOI: 10.1103/PhysRevA.110.023720

I. INTRODUCTION

Nonclassical states of light play a key role in various quantum technologies, ranging from quantum communications and information processing to quantum metrology. Their properties facilitate inherently secure cryptography [1–3], supremacy of quantum computing [4], and imaging and sensing with resolutions above classical limits [5,6]. An effective and experimentally suitable approach for the nonclassicality description is thus an indispensable ingredient enabling these technologies.

A quantum-optical state is considered nonclassical if its Glauber-Sudarshan P function is not positive semidefinite [7]. Based on this definition, various measures of single-mode nonclassicality have been proposed and studied, such as (1) the nonclassical distance [8], defined as the distance of a given state to the closest classical state, (2) the nonclassical depth [9,10], defined as the minimum amount of Gaussian noise required to convert a given nonclassical state into a classical one, and (3) entanglement potentials (EPs) [11]. The latter are studied in detail in this paper. For a comparative study of these nonclassicality measures see Ref. [12]. Moreover, nonuniversal criteria (often referred to as nonclassicality witnesses) are often applied in quantifying single- or multimode nonclassicality. These include the nonclassical volume [13], the Wigner distinguishability [14], and the potentials for quantum steering and Bell nonlocality [15], among dozens of other criteria (see, e.g., [16] and references therein). Here we apply the EPs, which have a number of advantages compared to other methods: (1) some of the EPs can be easily calculated (as shown in the following sections) contrary to, e.g., the nonclassical distance, (2) they can distinguish the nonclassicality degree of a wider variety of the classes of states compared to the nonclassical depth, (3) they are measurable, as we recently demonstrated experimentally [17], and (4) they are universal [11], as required for good nonclassicality measures, in contrast to nonclassicality witnesses. Thus, EPs prove to be a very convenient and experimentally feasible tool for describing and quantifying nonclassicality. This concept is built upon the ability of a nonclassical state to produce entanglement by interacting with purely classical states, usually the vacuum (see Fig. 1). An example of this effect is the single-photon state that transforms into a Bell state after interacting with the vacuum on a balanced beam splitter (BS).

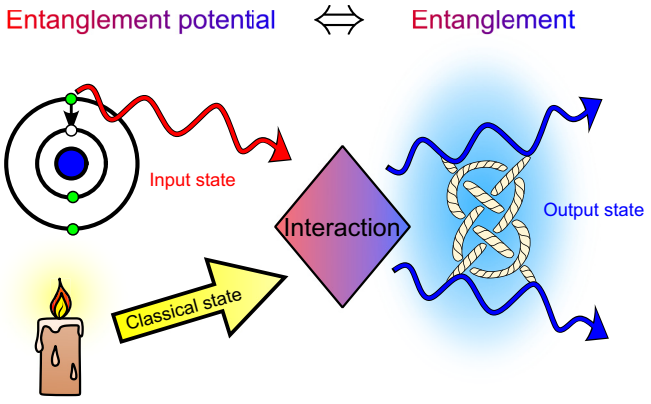

FIG. 1. Conceptual scheme of entanglement potentials. A tested state interacts with a purely classical state. The entanglement detected in the output two-mode state reveals the nonclassicality of the tested state and corresponds to its entanglement potential, as quantified by a chosen entanglement measure.

A practical benefit of EPs is that they exploit the well-developed formalism for the quantification of bipartite entanglement to describe single-mode nonclassicality. Moreover, any entanglement measure might be used to define the corresponding EP, thus allowing us to gain a deeper understanding of nonclassicality by studying mutual relations between various EPs. In this work, we focus on the EPs defined by the Wootters concurrence [18], the Peres-Horodecki negativity [19,20], and the relative entropy of entanglement (REE) [21].

This paper studies EPs, so it is related to our former theoretical [12,15,22] and experimental [17] works. However, we should emphasize that the results and their physical implications reported here are different from those described in our related experimental works [17], which focused on the relative potentials for entanglement, Einstein-Podolsky-Rosen (EPR) steering, and Bell nonlocality. In contrast to that work, we report here experimental relative EPs. Thus, this paper presents an experimental demonstration validating the theoretical predictions outlined in Refs. [12,22], while our previous experiment reported in [17] confirmed the concepts and predictions of Ref. [15].

Specifically, we experimentally generate maximally and minimally nonclassical single-photon states by quantifying their nonclassicality with relative EPs and refer to them as the relative nonclassicality measures of a single photon. By considering two EPs (say, EP1 and EP2) defined via different measures of entanglement, we refer to the maximal (minimal) relative EP1 vs EP2 if EP1 is maximized (minimized) with respect to a given value of EP2 for arbitrary single-qubit states. We experimentally demonstrate that we can increase the relative EPs for some entanglement measures by dissipation, thus experimentally confirming the predictions of Ref. [22], as well as some predictions of Refs. [12,23–25] on the bounds of relative entanglement measures.

The measured value of a given EP is affected by both the genuine properties of a tested state and the imperfections in its interaction with the chosen classical state. In this paper, we show that by analyzing the mutual relations among several EPs defined by standard entanglement measures, one can distinguish between these two effects. This capability makes the EPs a considerably more reliable tool for experimental nonclassicality quantification.

We support our theoretical predictions [22] with a proof-of-principle experiment on the platform of linear optics. In this experiment, we first generate the vacuum and one-photon superposition (VOPS) states that then interact with the vacuum on a BS. To avoid the need for the experimentally demanding vacuum detection, while reconstructing the output state, we encode the single-photon state into the horizontal polarization of a photon and the vacuum into its vertical polarization, which can be treated as a placeholder. We utilize the fact that a vertically polarized photon state has a vacuum component in its horizontal mode, i.e., $|0\rangle_H |1\rangle_V$, where the numbers denote the Fock states in the horizontal and vertical modes, respectively. For a more detailed description of the experimental implementation, see Sec. III.

II. NONCLASSICALITY QUANTIFIED BY ENTANGLEMENT POTENTIALS

A. Entanglement potentials

We calculate EPs for VOPS states, which can be described by the density matrix

$$\sigma(p,x) = \begin{pmatrix} 1-p & x \\ x^* & p \end{pmatrix} \tag{1}$$

expressed in the basis of the vacuum $|0\rangle$ and the Fock single-photon state $|1\rangle$, with p being the single-photon probability and x being a coherence term. Alternatively, one can write $x = e^{i\phi} D x_{\max}$, where $x_{\max} = \sqrt{(1-p)p}$ is the maximal possible absolute value of the coherence term, $D \in [0,1]$ is a dephasing factor, and $\phi \in [0, 2\pi)$ is an arbitrary phase. The dephasing factor can be interpreted by assuming a pure state affected by a dephasing channel, with a phase-flip probability of f; then $D = |1-2f|$.

Assuming a given VOPS state at one port of a BS and the vacuum state at the other port, the output density matrix reads [15]

$$\rho_{wr}(p,x) = \begin{pmatrix} 1-p & -wrx & wtx & 0 \\ -wrx^* & pr^2 & -pw^2rt & 0 \\ wtx^* & -pw^2rt & pt^2 & 0 \\ 0 & 0 & 0 & 0 \end{pmatrix}, \tag{2}$$

given in the standard computational basis $\{|00\rangle, |01\rangle, |10\rangle, |11\rangle\}$, where r and t are the reflection and transmission coefficients, respectively. Due to the fact that the phases of r and t do not affect any reasonable entanglement measure, we assume they are both real non-negative. We assume that both output ports of the BS are uniformly affected by phase damping (see Appendix A 7), as described by the phase-damping parameter $\kappa \equiv \kappa_1 = \kappa_2$ or, equivalently, the parameter $w = \sqrt{1-\kappa}$ for $w, \kappa \in [0,1]$, where $w = 1$ corresponds to a perfectly coherent interaction.

The matrix in Eq. (2) can be used to calculate any entanglement measure. In this paper, we use the negativity, the concurrence, and the REE to quantify the output state entanglement.

The negativity [19,26,27], which is related to the Peres-Horodecki entanglement criterion, is defined for a two-qubit state ρ as either zero or the absolute value of the smallest negative eigenvalue of a partially transposed density matrix and is multiplied for convenience by a factor of 2:

$$N(\rho) = \max[0, -2 \min \mathrm{eig}(\rho^\Gamma)], \tag{3}$$

where the superscript Γ denotes partial transposition.

The Wootters concurrence can be calculated using the formula [18]

$$C(\rho) = \max\left(0, 2\lambda_{\max} - \sum_j \lambda_j\right), \tag{4}$$

where $\lambda_j^2 = \mathrm{eig}[\rho(Y \otimes Y)\rho^*(Y \otimes Y)]$, $\lambda_{\max} = \max_j \lambda_j$, the asterisk $(*)$ denotes complex conjugation, and Y is a Pauli operator.

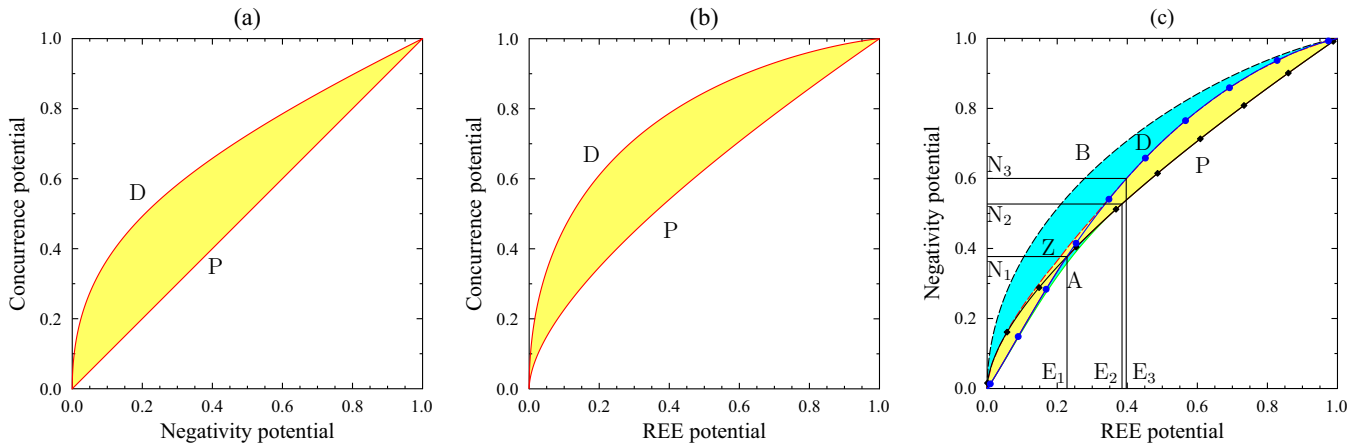

FIG. 2. Relative entanglement potentials: (a) $\mathrm{CP}_{wr}(\sigma)$ vs $\mathrm{NP}_{wr}(\sigma)$, (b) $\mathrm{CP}_{wr}(\sigma)$ vs $\mathrm{REEP}_{wr}(\sigma)$, and (c) $\mathrm{NP}_{wr}(\sigma)$ vs $\mathrm{REEP}_{wr}(\sigma)$ for arbitrary single-qubit states σ. Note that the two-qubit states ρ_{wr}, which can be generated from σ by a balanced BS ($t = r = 1/\sqrt{2}$) and assuming no damping ($w = 1$) in a perfect EP-detection setup, are located in the yellow regions. By contrast to this, the cyan regions in (c) indicate those ρ_{wr} which cannot be generated from σ in this way; their generation requires an additional resource, i.e., a tunable BS with $t \neq r$, amplitude, or phase damping ($w < 1$). Characteristic points are plotted at ($E_1 \approx 0.228, N_1 \approx 0.377$), ($E_2 \approx 0.385, N_2 \approx 0.527$), and ($E_3 \approx 0.397, N_3 \approx 0.6$). Their meaning is explained in the text.

The REE [21] is another popular two-qubit entanglement measure and is defined as

$$\mathrm{REE}(\rho) = S\left(\rho \middle|\middle| \rho_{\mathrm{sep}}^{\mathrm{opt}}\right) \equiv \min_{\rho_{\mathrm{sep}} \in \mathcal{D}} S(\rho||\rho_{\mathrm{sep}}) \tag{5}$$

in terms of the Kullback-Leibler distance, $S(\rho||\rho_{\mathrm{sep}}) = \mathrm{Tr}(\rho \log_2 \rho - \rho \log_2 \rho_{\mathrm{sep}})$, of a given two-qubit state ρ from the closest separable state $\rho_{\mathrm{sep}}^{\mathrm{opt}}$, where $\mathcal{D}$ is the set of all two-qubit separable states ρ_{sep}.

Thus, one can define the negativity potential (NP), the concurrence potential (CP), and the relative entropy of entanglement potential (REEP) as

$$\mathrm{NP}_{wr}[\sigma(p,x)] = N[\rho_{wr}(p,x)], \tag{6}$$

$$\mathrm{CP}_{wr}[\sigma(p,x)] = C[\rho_{wr}(p,x)], \tag{7}$$

$$\mathrm{REEP}_{wr}[\sigma(p,x)] = \mathrm{REE}[\rho_{wr}(p,x)], \tag{8}$$

respectively. In particular, these generalized EPs reduce to the standard ones assuming a balanced BS (with $t = r$) and no damping ($w = 1$). Note that the potential is attributed to the single-mode state σ by evaluating the entanglement of the two-mode state ρ.

We highlight again that to acquire a "true" EP of the input state one needs to have a balanced ($r = t = 1/\sqrt{2}$) and lossless ($w = 1$) BS; otherwise, the values of the observed EPs are diminished due to imperfect interactions. Simultaneously, such imperfect interactions can increase relative EPs; thus, they can be considered a resource, as explained in detail below.

B. Relative entanglement potentials

We refer to the *relative entanglement potentials* and *relative nonclassicality* of a single-mode state when considering an EP for a given value of another EP calculated for the same state. Specifically, we study the following relative EPs: the CP vs NP, CP vs REEP, and NP vs REEP and vice versa, as shown in Fig. 2.

The yellow regions in all the panels of Fig. 2 show the allowed values of the relative EPs for arbitrary single-photon states assuming a perfectly balanced ($t = r$) and lossless BS. As predicted theoretically in Ref. [22], the cyan regions in Fig. 2(c) can be reached by relative EPs only for imperfect BSs, e.g., assuming their phase damping, amplitude damping, or unbalanced splitting.

Note that a straight line is observed for pure states when comparing the CP and NP, as shown in Fig. 2(a). However, the REEP is defined by logarithms, while the CP and NP are not. Thus, straight lines are not observed for pure states in Figs. 2(b) and 2(c).

This work reports our experimental generation and tomographic detection of (1) the states in the cyan regions of Fig. 2(c) and (2) the states close to the maximally nonclassical states, which are explicitly defined in the Appendix.

III. EXPERIMENTAL SETUP

We constructed an experimental setup on the platform of linear optics (see Fig. 3). As mentioned above, we employ polarization encoding, where the horizontal component of the polarization represents the single-photon state while the vertically polarized component represents the vacuum state.

Separable photon pairs are generated using a type-I spontaneous parametric down-conversion (SPDC). One photon from each pair is guided through an optical fiber into the *single-qubit-preparation* stage. There, using a set of motorized quarter-wave (QWP) and half-wave (HWP) plates, the photon is transformed into any pure single-qubit state in the form of Eq. (1) with $D = 1$. To tune the value of D, a set of two beam displacers (BDs) with a half-wave plate rotated by 45° in the middle is used. The second BD can by tilted by a piezoactuator, allowing us to set a path difference and thus a phase shift $\Delta\phi$ between the two polarization

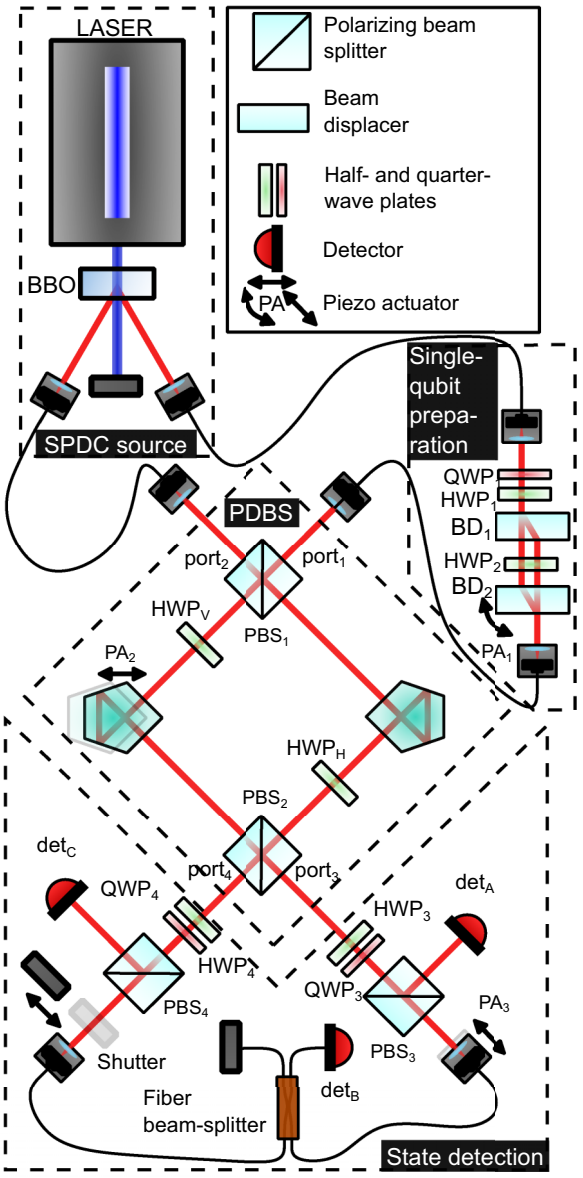

FIG. 3. Scheme of the experimental setup. SPDC stands for spontaneous parametric down-conversion, BBO denotes beta barium borate (β-BaB_2O_4) crystal, and PDBS stands for polarization-dependent beam splitter.

components. By changing randomly, with probability f, between the identity ($\Delta\phi = 0$) and the phase-flip ($\Delta\phi = \pi$) operations, a desired value of D is achieved. The single qubit is then guided through another optical fiber into the first port of the polarization-dependent beam splitter (PDBS). The second photon from each pair is vertically polarized, as it plays the role of the vacuum, and is guided directly from the SPDC source into the second port of the PDBS.

The PDBS allows for independent tuning of the beam-splitting ratio for the horizontal and vertical polarization modes. The PDBS is implemented by means of a Mach-Zehnder interferometer composed of two polarizing beam splitters (PBSs) with a motorized HWP in each arm. The horizontal (vertical) polarization components of both photons meet in arm_H (arm_V) after implementing a bit-flip operation to one of the inputs (HWP_2).

For example, a vertically polarized photon from port_2 is transmitted through PBS_1, while a vertically polarized photon from port_1 is first transformed, via the bit-flip operation, into a horizontally polarized photon and subsequently reflected by PBS_1. At this point the originally vertical polarization components of the first and second input modes are directed into the same spatial mode with the horizontal and vertical polarizations, respectively. Subsequently, these modes impinge on HWP_V, which acts on these polarization modes identically to a tunable BS acting on spatial modes. Mixing the polarization states in the arms intertwines the signal from different inputs; therefore, the reflection coefficients for each polarization component are set by the rotation of the wave plates: $r_{\text{H;V}} = \sin(2\theta_{\text{H;V}})$. The rotation of HWP_3 is offset by 45° to compensate for the initial bit-flip operation. For all measurements, θ_V is set to 22.5°, accomplishing a balanced splitting for the vertical polarization component, corresponding to the symmetric behavior of the vacuum on a BS, while θ_H is tuned.

Because a HWP rotated by 22.5° serves as a balanced beam splitter for the polarization components, the originally vertically polarized photons, which are directed by PBS_1 into the same spatial mode as orthogonal polarizations, are subjected to the Hong-Ou-Mandel effect $|H\rangle\,|V\rangle \rightarrow (|H\rangle\,|H\rangle - |V\rangle\,|V\rangle)/\sqrt{2}$. Thus, both the vacuum placeholders are bunched at the output of PBS_2.

Note that the rotation of HWP_H enables us to achieve the optimal splitting ratio for the horizontal polarization; we set the rotation by 22.5° for balanced splitting. However, in this experiment, we also investigate the effect of an imperfect interaction upon the studied potentials. Then, the splitting ratio for the horizontal polarization, representing the single-photon component, is tuned by rotating HWP_H.

Due to the specific nature of the applied encoding, which implies the bunching at a BS of vertically polarized photons corresponding to the vacuum, we cannot use standard quantum tomography. We designed a special detection apparatus and procedure to reconstruct the output-state density matrix. The detection apparatus consists of a set of wave plates followed by a polarizing BS in both output ports of the PDBSs. One output port of each of these splitters is guided directly to a single-photon detector, while the other is led to a fiber BS, whose one output is then guided to a third detector. Using coincidence logic, events consisting of simultaneous detections by two detectors are registered.

The reconstructed density matrix takes the form

$$\rho_{\text{out}} = \begin{pmatrix} \rho_{11} & \rho_{12} & \rho_{13} & 0 \\ \rho_{21} & \rho_{22} & \rho_{23} & 0 \\ \rho_{31} & \rho_{32} & \rho_{33} & 0 \\ 0 & 0 & 0 & 0 \end{pmatrix} = \begin{pmatrix} M_A & M_C & M_D & 0 \\ M_C^* & & & 0 \\ M_D^* & & \boldsymbol{M_B} & 0 \\ 0 & 0 & 0 & 0 \end{pmatrix},$$

$$M_B = \begin{pmatrix} \rho_{22} & \rho_{23} \\ \rho_{32} & \rho_{33} \end{pmatrix}, \tag{9}$$

where $\mathbf{M}_B$ is a 2×2 matrix, and we assume only the absolute value of the off-diagonal elements because any state in Eq. (2) can be transformed into a fully

positive matrix using only local rotations and, as a result, the entanglement measures are independent of the phases in ρ_{out}.

We split the detection procedure into several steps corresponding to the blocks in the matrix in Eq. (9). The term M_A corresponds to the case of two vertically polarized photons on the input. Due to the rotation of HWP_V and the Hong-Ou-Mandel effect [28], such photons bunch at the output of the PDBS, meaning they are both in one output port or the other. Because they propagate symmetrically in both arms and the vertical polarization serves only as a placeholder for the vacuum, we register the signal only in one arm and correct for the undetected signal accordingly. The term is measured using detectors det_A and det_B, while the shutter in port_4 is closed and wave plates in port_3 are set, so that the bunched photons split in half of the cases. Overall, the measured signal is multiplied by a factor of 4 (a factor of 2 from focusing only on one output arm and another factor of 2 due to the splitting probability).

The term M_B corresponds to the case of one horizontally polarized photon in either port_3 (ρ_{22}) or port_4 (ρ_{33}) and the coherence factor between these cases (ρ_{23}). The vertically polarized component propagates symmetrically in both output arms. In this case, we register the vertically polarized component in the output port where the horizontal component is not detected. To correct for neglecting the vertical component in the other arm, we multiply the signal by the factor of 2. The submatrix M_B itself is measured by standard two-qubit state tomography [29,30] using det_A and det_C, and a maximum-likelihood estimation is applied. This leads to a matrix of the form

$$\rho_B = \begin{pmatrix} 0 & 0 & 0 & 0 \\ 0 & & & 0 \\ 0 & & \tilde{M}_B & 0 \\ 0 & 0 & 0 & 0 \end{pmatrix}, \tag{10}$$

where $\tilde{M}_B$ is the normalized M_B. A proper renormalization takes into account the measurement of M_A.

The terms M_D and M_C in Eq. (9) are calculated directly from the visibility v of the interference pattern, which is related to the coherence term $v(\rho_{11} + \rho_{33})/2 = |M_D|$, while the position of the interference pattern corresponds to the phase of M_D. Thus, to acquire the M_D term, we measure directly the coherence between ρ_{11} and ρ_{33} via an interference pattern on the fiber BS using the detectors det_A and det_B. In port_3, we project onto the term ρ_{11} using the same setting as when measuring M_A. In port_4, the shutter is left open, and the wave plates are set such that the term ρ_{33} is projected onto the same set of detectors, leading to the interference of the two projected terms. A piezo-driven phase shifter (PA_3) is used to sweep through the whole interference pattern, whose maxima and minima can be used to calculate the absolute value of the coherence term. Note that due to the instability of the interferometer formed by the PBS_2 and a fiber BS, it is impossible to precisely determine the phase of M_D. Fortunately, this is unnecessary for our purposes. On the other hand, precise determination of the maxima and minima of an interference pattern is guaranteed by sweeping multiple times through the pattern. Using the same measurement method with settings symmetrically swapped for port_3 and port_4, we acquire the value of M_C. For more details about the measurement procedure, see [17], where we used this setup for a conceptually different experiment.

The applied tomography method includes several modifications compared to typical two-qubit tomography schemes (see, e.g., [31–34] and references therein). The key difference lies in the fact that in this experiment, the cases when both photons leave the PBS_2 at the same output port must be detected in order to evaluate all the components of a given density matrix. This is not the case in typical two-qubit tomography, in which measurement is performed solely on the coincidences across the output ports. This difference constitutes the reason for the step-by-step reconstruction of the density matrix from the blocks described in Eq. (9). Specifically, the off-diagonal terms have to be evaluated by adding a fiber coupler superimposing the output ports. We benefit from the fact that the phase value of these components does not have any physical impact on the evaluated entanglement measures. As a result the interferometer formed by PBS_2 and this fiber coupler is not required to be phase stable, and only the interference visibility needs to be measured. A maximum-likelihood procedure is used in the final stage of the estimation to ensure the physicality of the reconstructed density matrices. A similar procedure requiring an additional fiber coupler and a step-by-step reconstruction of the density measurement was successfully tested before, e.g., to verify the preparation of the two-photon Knill-Laflamme-Milburn states [35,36].

At the end of this section, let us also explain the difference between our current experiment and that reported in Ref. [17]: (1) We are effectively using the old experimental setup, which, however, now encompasses an unbalanced splitting of photons and the possibility of incoherent interactions. Specifically, the difference is that the wave plate HWP_H within the PDBS device is varied to introduce the incoherent interaction, whereas it remained at a fixed setting in Ref. [17]. Thus, tunability was possible with the previous setup; however, it was not explored since that was not the goal of our previous experiment. (2) We perform measurements of new classes of states. Specifically, the states that have undergone imperfect interaction, i.e., with an unbalanced beam-splitting ratio and controllable incoherent interactions. (3) We perform a previously unused postprocessing of the measured states. Specifically, we apply a probabilistic mixing of the registered counts for HWP_H rotated to $\pm 22.5^\circ$ in order to achieve the incoherent beam splitting.

IV. EXPERIMENTAL RESULTS

Here we analyze the following experimentally obtained classes of states: (i) pure input states and coherent interaction with the vacuum (for the BS parameters $r \in [0, 1]$ and $w = 1$), (ii) dephased input states and coherent interaction with the vacuum, and (iii) a one-photon state subjected to an incoherent interaction with the vacuum with a varying incoherence parameter. For the ranges of density-matrix parameters see Table I.

To verify that the setup is properly adjusted and the produced states qualify as class (i), we put a condition on the

TABLE I. Classes of experimentally measured states, where p is the single-photon probability, x is the coherence parameter, $x_{\max} = \sqrt{p(1-p)}$ is the maximum value of the coherence parameter, r is the reflectivity amplitude, and w characterizes the output state coherence.

	Class of states	p	x	r	w
(i)	Pure input	[0,1]	$x_{\max}$	[0,1]	1
(ii)	Dephased input	[0,1]	0	$1/\sqrt{2}$	1
(iii)	Incoherent interaction	1	$0 = x_{\max}$	$1/\sqrt{2}$	[0,1]

value of the off-diagonal terms: $\sqrt{\rho_{12}/\rho_{12}^{\max}}\sqrt{\rho_{13}/\rho_{13}^{\max}} > 0.5$, where $\rho_{1j}^{\max} = \sqrt{\rho_{11}\rho_{jj}}$ is the maximal possible value of ρ_{1j} given the values of ρ_{11} and ρ_{jj} for $j \in \{2, 3\}$.

The incoherent interaction needed to prepare states of class (iii) was achieved by randomly swapping θ_H between $\pm 22.5^\circ$ and summing the registered coincidence counts.

For all of the output states, we calculated the three entanglement measures: the negativity, the concurrence, and the REE. All these quantities were estimated with uncertainties typically below 0.03. In Fig. 4, we plot their mutual relations for the measured states. In these three plots, the white area represents mutual relations that are unphysical for any two-qubit state. In Fig. 4(a) we show the mutual relation between the negativity and the concurrence for the experimental states. This relation allows us to separate dephased input states from pure input states independently of the (in)coherence of the interaction. For a better understanding, this plot depicts theoretical loci for states of various parameters D and w.

Figure 4(a) shows that our experimentally generated states are located relatively close to the theoretical lower boundary states (labeled P) for any values of NP. Even though the experimental states dephased at the input [class (ii)] do not lie exactly on the opposing boundary D, they are clearly separated from the other classes. Moreover, Fig. 4(b) shows the relation between the concurrence and the REE. States of class (iii) do cover the boundary line B as theoretically predicted. On the other hand, the experimental states of classes (i) and (ii) do not correspond exactly to the theoretical boundaries P and D, respectively. Nevertheless, they can be mutually separated by the boundary line B.

Figure 4(c) demonstrates distinct regions of physically possible EPs. The yellow inner region represents the EPs attainable with any input state interacting on a balanced and lossless BS. The cyan areas are achievable only if the interaction is incoherent (larger upper area) or the BS is unbalanced (small lower area). As a result, by analyzing the mutual relation between the REE and the negativity, we can clearly uncover imperfections in the interaction. It is seen that states of class (iii) are located in the cyan region, while all the other states remain in the yellow region (up to experimental imperfections). Note that the smaller cyan area on the right-hand side is theoretically reachable by unbalanced beam splitting. In experiment, this area proved to be unattainable because the area is very small and dephasing of the output (and other experimental imperfections) pushes the states to the left-hand side of the plot. This shortcoming, however, does not diminish the main point shown by this plot. Observing EPs outside of the yellow area signals imperfections in the BS interaction and warns that the observed potentials underestimate the true values of EPs of the tested states.

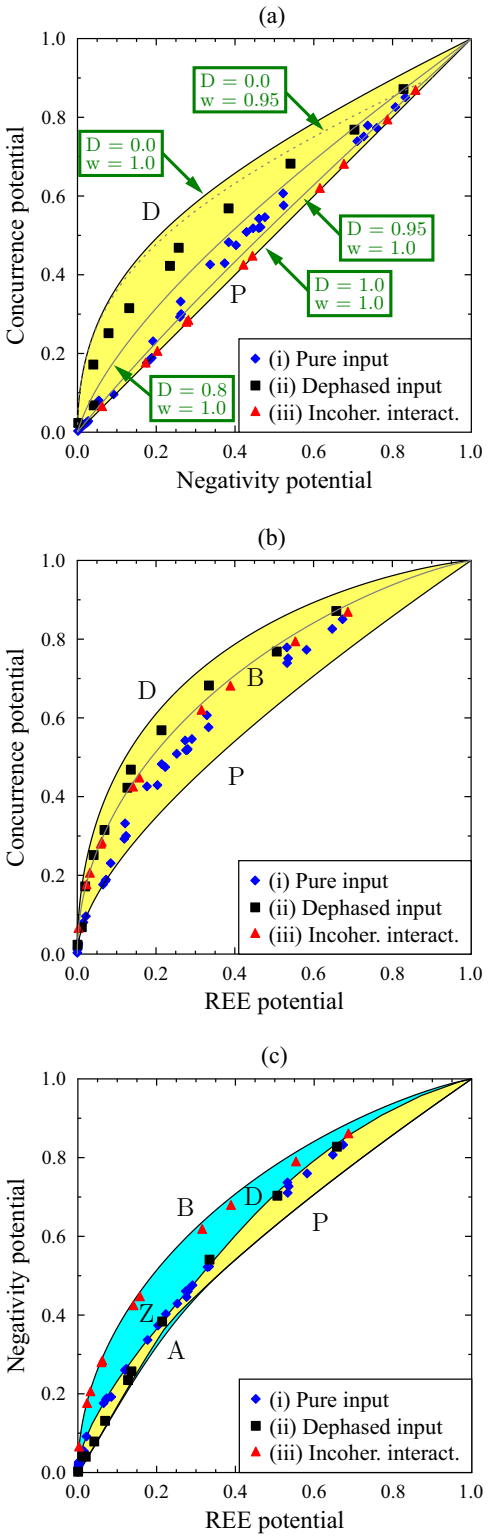

FIG. 4. Relative entanglement potentials defined by various entanglement measures for the experimental states representing classes (i)–(iii). The gray middle curve in (c) corresponds to our theoretical predictions for the states in class (iii).

Therefore, these relations allow us to distinguish between the three tested classes of states. The relation between the CP and the NP distinguishes classes (i) and (iii) from class (ii), while the relation between the REEP and the NP distinguishes classes (i) and (ii) from class (iii).

Finally, one can observe in Fig. 4(c) that our experimentally generated states are located relatively close to theoretical boundary states A, B, Z, D, and even P for some ranges of the NP. But we must admit that we failed to generate high-quality pure states P for NP > 0.4. We note that all the raw and processed experimental data, along with the processing scripts, are provided in the Supplemental Material [37].

V. DISCUSSION AND CONCLUSIONS

We both theoretically and experimentally analyzed the relations among the three EPs for various classes of states. These include the potentials: REEP, CP, and NP. Specifically, we compared CP and NP, CP and REEP, and NP and REEP for experimentally generated and tomographically reconstructed states. Our experimental results are consistent with previous theoretical expectations in the sense of relative EPs reachable by states belonging to these classes.

We conducted different experiments using essentially the same optical setup as that used in Ref. [17]. Therefore, the main differences from the previous experiment lie in the results (obtained here for both balanced and unbalanced splitting of photons) and their interpretation. Specifically, we experimentally generated single-qubit states close to those with maximal and minimal relative EPs. Note that Ref. [17] focused on showing the feasibility of our experimental setup for demonstrating the hierarchy of the potentials for quantum entanglement, EPR steering, and Bell nonlocality.

In our experiments, we employed photon polarization instead of photon-number encoding, which is typically considered for the determination of EPs. Specifically, we assumed that the horizontal and vertical components of polarization states represent the single-photon and vacuum states, respectively. We emphasize again that the applied polarization encoding serves as an effective analog to the encoding of VOPS states, significantly simplifying their physical realization. Indeed, polarization encoding offers a much simpler approach than photon-number encoding or single-rail encoding, which are affected by photon loss and dark counts. Nevertheless, the use of polarization encoding does come with its own experimental challenges. Most notably, an imperfect polarization adjustment using polarization encoding may manifest as photon creation in the framework of the VOPS states. We minimize this adverse effect by fine tuning of the setup and by adding polarizers to the input, thus purifying the polarization states obtained from the two-photon source. It should be pointed out that a similar problem arises in the genuine VOPS encoding considering that single-photon detection is burdened by dark detection events. Photon loss that cannot be easily prevented poses a significant challenge to the implementation of VOPS states. This issue does not affect the results obtained in the polarization encoding because of the postselection on two-photon detection events. Thus, we can overcome the majority of technological losses which are polarization independent, including fiber coupling, back-reflection, absorption on imperfect components, and detector efficiency.

Based on the experimentally reconstructed two-qubit states generated from single-photon states, we determined the EPs defined by the Peres-Horodecki negativity, the Wootters concurrence, and the relative entropy of entanglement. Among our experimental states we were able to find those which are very close to the theoretical upper and lower bounds of the relative EPs, as predicted in Refs. [12,15,22].

Moreover, we confirmed experimentally the counterintuitive theoretical result of Ref. [22] that the NP for given values of the REEP can be increased by dissipation. We note that our improved experimental setup, in contrast to that of Ref. [17], enables performing unbalanced splitting of photons and the possibility of introducing controllable incoherent interactions. This is accompanied by postprocessing of the measured state, which was not used in the previously reported experiment.

We documented the benefits of studying the relations between EPs, as they allow us to detect imperfect interaction between the tested state and the classical state. Detecting imperfections in the interaction is critical in preventing misjudging the states' true nonclassicality. Considering that imperfections are unavoidable in experimental reality, especially in near-future quantum technologies, we believe that our findings are relevant for the practical deployment of EPs as a method for nonclassicality quantification.

Further analysis could be performed to allow us to establish markers of various interaction flaws (unbalanced beam splitting, decoherence, and amplitude damping). One could, for instance, immediately deduce the incoherence of the interaction by comparing the absolute value of the term ρ_{12} to its maximum value $\rho_{12}^{\max}$. Our analysis, however, enables us to estimate the impact of this incoherence on the observed EPs.

ACKNOWLEDGMENTS

J.K. gratefully acknowledges the support from Project No. IGA_PrF_2024_004 of Palacký University. A.Č. and K.L. acknowledge support from Project No. OP JAC CZ.02.01.01/00/22_008/0004596 of the Ministry of Education, Youth, and Sports of the Czech Republic. K.B. and A.M. were supported by the Polish National Science Centre (NCN) under Maestro Grant No. DEC-2019/34/A/ST2/00081. We thank Cesnet for data management services.

APPENDIX: MAXIMALLY NONCLASSICAL SINGLE-QUBIT STATES

Here we recall, after Refs. [12,22], definitions of maximally nonclassical single-qubit states and their corresponding two-qubit states, which are located at the upper or lower theoretical bounds of various relative EPs, as shown in Figs. 2 and 4. Note that Appendix A 1 to A 4 define the boundary state for the yellow area in Figs. 2 and 4, while the remaining sections define the boundary states for the extended cyan area.

1. Pure states σ_{P}

First, we consider single-qubit pure states,

$$|\psi_p\rangle = \sqrt{1-p}\,|0\rangle + e^{i\phi}\sqrt{p}\,|1\rangle\,, \tag{A1}$$

which are nonclassical for any $p \in (0, 1]$. Note that $\sigma_{\rm P} \equiv |\psi_p\rangle\langle\psi_p|$ is a special case of Eq. (1) for $|x| = \sqrt{p(1-p)} = x_{\max}$ and $\phi = {\rm Arg}(x)$. An arbitrary pure state $|\psi_p\rangle$, after being mixed with the vacuum at the balanced and lossless BS, is transformed into the entangled states for $p \neq 0$:

$$|\Psi_{\rm out}(p)\rangle = \sqrt{1-p}|00\rangle + \sqrt{\frac{p}{2}}(|10\rangle - |01\rangle), \tag{A2}$$

which reduces to the singlet state for $p = 1$. The EPs are simply given by

$$\begin{aligned} {\rm REEP}(\sigma_{\rm P}) &= h\left(\tfrac{1}{2}[1+\sqrt{1-p^2}]\right), \\ {\rm CP}(\sigma_{\rm P}) &= {\rm NP}(\sigma_{\rm P}) = p, \end{aligned} \tag{A3}$$

where h is the binary entropy.

As seen in Fig. 2, single-qubit pure states are the maximally nonclassical states corresponding to the upper bounds for (1) the NP and (2) the REEP as a function of CP $\in [0, 1]$, as well as (3) the REEP as a function of NP $\in [N_2, 1]$, where $N_2 \approx 0.527$.

Moreover, on the scale of Fig. 2(c), we cannot see any differences between the curves for the pure states σ_P and the optimally dephased states σ_Z, as defined below, if NP $< N_0 \approx 0.2$. Experimentally, these σ_P and σ_Z cannot be distinguished for this range of NP. Thus, effectively, pure states can also be considered maximally nonclassical in terms of (4) the largest NP as a function of the REEP for NP $\in [0, N_0]$, where $N_0 \approx 0.2$ assuming a balanced and lossless BS.

2. Completely dephased states $\sigma_{\rm D}$

Completely dephased single-qubit states, which are also referred to as completely mixed states [12,22], are the mixtures of $|0\rangle$ and $|1\rangle$ corresponding to the special case of Eq. (1) for the vanishing coherence parameter $x = 0$, i.e.,

$$\sigma_{\rm D} = \sigma(p, x = 0) = (1-p)\,|0\rangle\langle 0| + p\,|1\rangle\langle 1|\,. \tag{A4}$$

We recall that $\sigma_{\rm D}$ is transformed by the balanced and lossless BS (with the vacuum in the other port) into the Horodecki state,

$$\rho_{\rm H}(p) = \rho_{\rm out}(p, 0) = p\,|\Psi^-\rangle\langle\Psi^-| + (1-p)\,|00\rangle\langle 00|\,, \tag{A5}$$

which is a mixture of the singlet state, $|\Psi^-\rangle = (|10\rangle - |01\rangle)/\sqrt{2}$, and the vacuum. The entanglement (as well as EPR steering and Bell nonlocality) of the two-photon Horodecki states has been studied intensively (see, e.g., Refs. [20,38,39] and references therein). The EPs for $\rho_{\rm D}$ thus correspond to the known entanglement measures of the Horodecki states [25]:

$$\begin{aligned} {\rm REEP}(\rho_{\rm D}) &= (p-2)\log_2\left(1-\frac{p}{2}\right) + (1-p)\log_2(1-p), \\ {\rm NP}(\rho_{\rm D}) &= \sqrt{(1-p)^2+p^2} - (1-p), \end{aligned} \tag{A6}$$

and ${\rm CP}(\rho_{\rm D}) = p$.

The completely dephased states $\rho_{\rm D}$, as shown in Fig. 2, are the maximally nonclassical single-qubit states with respect to the largest values of (1) the CP as a function of NP $\in [0, 1]$, (2) the CP vs REEP $\in [0, 1]$, (3) the REEP vs NP $\in [0, N_0]$, where $N_0 \approx 0.2$, and (4) assuming a balanced and lossless BS, the NP vs REEP $\in [E_3, 1]$, where $E_3 = 0.397$.

3. Optimally dephased states $\sigma_{\rm Z}$

Optimally dephased single-qubit states, which maximize the NP for a given value of the REEP assuming a perfectly balanced and lossless BS in an EP setup, are defined as [22]

$$\sigma_{\rm Z}(\bar{N}) = \sigma[p_{\rm opt}, x_{\rm opt} = f(p_{\rm opt}, \bar{N})], \tag{A7}$$

where, for brevity, we denote $\bar{N} \equiv$ NP and

$$f(p, \bar{N}) = \tfrac{1}{2}\sqrt{(1+p/\bar{N})[2\bar{N}(\bar{N}+1) - (\bar{N}+p)^2]}. \tag{A8}$$

The optimal probability $p_{\rm opt}$ is found numerically by minimizing

$${\rm REEP}\{\sigma[p_{\rm opt}, f(p_{\rm opt}, \bar{N})]\} = \min_p {\rm REEP}\{\sigma[p, f(p, \bar{N})]\}. \tag{A9}$$

Here, the minimization is performed for $p \in [\bar{N}, \sqrt{2\bar{N}(\bar{N}+1)} - \bar{N}]$ for a given $\bar{N}$. It is seen in Fig. 2(c) that $\sigma_{\rm Z}(\bar{N})$ is practically indistinguishable from $\sigma_{\rm D}$ for $\bar{N} > N_3 \approx 0.6$ or, equivalently, for REEP $> E_3 \approx 0.397$. Moreover, $\sigma_{\rm Z}(\bar{N})$ goes into pure states $\sigma_{\rm P}$ for small $\bar{N}$ (say, $\bar{N} \lesssim 0.2$). Thus, these partially dephased states become completely dephased for large EPs and completely purified for small EPs. However, $\sigma_{\rm Z}(\bar{N})$ is clearly different from both $\sigma_{\rm P}$ and $\sigma_{\rm D}$ for $\bar{N}$ close to $N_1 \approx 0.377$.

4. Optimally dephased states $\sigma_{\rm Y}$

Note that there exist optimally dephased single-qubit states (say, $\sigma_{\rm Y}$) when comparing the NP and the REEP in Fig. 2(c), for which ${\rm NP}(\sigma_{\rm Y})$ has slightly lower values than both ${\rm NP}(\sigma_{\rm D})$ and ${\rm NP}(\sigma_{\rm P})$, especially near the crossing at $N_1 \approx 0.377$ of the curves for ${\rm NP}(\sigma_{\rm D})$ and ${\rm NP}(\sigma_{\rm P})$. Nevertheless, the states ${\rm NP}(\sigma_{\rm Y})$ cannot be distinguished from ${\rm NP}(\sigma_{\rm D})$ (if NP $\leqslant N_1$) and ${\rm NP}(\sigma_{\rm D})$ (if NP $\geqslant N_1$) on the scale of Fig. 2(c); therefore, due to experimental uncertainty, they also cannot be distinguished experimentally. Thus, $\sigma_{\rm Y}$ are not discussed in detail in this paper, and consequently, $\min[{\rm NP}(\sigma_{\rm D}), {\rm NP}(\sigma_{\rm P})]$ are considered to be an effective lower bound for the NP vs REEP assuming a balanced and lossless BS in our setup.

5. Boundary states $\rho_{\rm A}$ by unbalanced beam splitting

The above four classes of two-qubit states can be generated from single-qubit states assuming a perfectly balanced and lossless BS ($\theta = \pi/2$) in an ideal EP-detection scheme. Here we assume that the BS can be tuned to change its reflectivity, $R = r^2 = \sin^2(\theta/2)$, and transmissivity, $T = t^2 = \cos^2(\theta/2)$. Then, a completely dephased state $\sigma_{\rm D} = \sigma(p, x = 0)$ is transformed by a tunable BS into the generalized Horodecki state [22]:

$$\begin{aligned} \rho^{\theta}_{\rm out}(p, x = 0) &= p|\Psi_q\rangle\langle\Psi_q| + (1-p)|00\rangle\langle 00| \\ &\equiv \rho_{\rm GH}(p, q = R), \end{aligned} \tag{A10}$$

where $p, q \in [0, 1]$ and

$$|\Psi_q\rangle = \sqrt{q}|01\rangle - \sqrt{1-q}|10\rangle. \tag{A11}$$

The boundary states ρ_A, which are shown in Figs. 2(c) and 4(c), are given as

$$\rho_{\rm A}(\bar{N}) = \rho_{\rm GH}[\bar{p}_{\rm opt}, \bar{q}_{\rm opt}], \tag{A12}$$

where $\bar{q}_{\rm opt} = f_1(\bar{p}_{\rm opt}, \bar{N})$ and

$$f_1(p, \bar{N}) = \frac{1}{2p}[p \pm \sqrt{p^2 - \bar{N}^2 - 2\bar{N}(1-p)}], \tag{A13}$$

for the optimized value of the mixing parameter $\bar{p}_{\rm opt}(\bar{N})$, which can be found numerically such that

$$\mathrm{REE}\{\rho_{\rm GH}[\bar{p}_{\rm opt}, \bar{q}_{\rm opt})]\} = \max_p \mathrm{REE}\{\rho_{\rm GH}[p, f_1(p, \bar{N})]\}. \tag{A14}$$

Here, the maximization is performed for such p given $\bar{N}$ that $f_1(p, \bar{N}) \in [0, 1]$.

6. Boundary states $\rho_{\rm A}$ by amplitude damping

Here we describe another method for generating the boundary states $\rho_{\rm A}$, where instead of an unbalanced BS, as described above, we use again a balanced BS but allow for amplitude damping.

A single-qubit pure state $|\psi_p\rangle$ is transformed by a balanced BS into $|\Psi_{\rm out}(p)\rangle$, given by Eq. (A2). By applying local unitary transformations, $|\Psi_{\rm out}(p)\rangle$ can be converted into $|\Psi_q\rangle$ [40], given by Eq. (A11), where $q = (1 - \sqrt{1-p^2})/2$, without changing its entanglement, as $C(|\Psi_{\rm out}\rangle) = C(|\Psi_q\rangle) = 2\sqrt{q(1-q)} = p$.

Let us assume now that each qubit ($i = 1, 2$) in $|\Psi_q\rangle$ undergoes amplitude damping, as described by the standard Kraus operators [4]:

$$E_0(\gamma_i) = |0\rangle\langle 0| + \sqrt{1-\gamma_i}|1\rangle\langle 1|, \quad E_1(\gamma_i) = \sqrt{\gamma_i}|0\rangle\langle 1|, \tag{A15}$$

with γ_i being amplitude-damping coefficients. Then a pure state $|\Psi_q\rangle$ for any $q \in [0, 1]$ is transformed into the generalized Horodecki state [25,41]:

$$\begin{aligned}\rho_{\rm ADC}(q, \gamma_1, \gamma_2) &= \rho_{\rm GH}(p', q') \\ &= p'|\Psi_{q'}\rangle\langle\Psi_{q'}| + (1-p')|00\rangle\langle 00|,\end{aligned} \tag{A16}$$

where $p' = 1 - (1-q)(1-\gamma_1) - q(1-\gamma_2)$ and $q' = q[(1-\gamma_2)/(1-p')]$. Thus, to generate a boundary state ρ_A, we optimize p' according to Eqs. (A12)–(A14), where p and q should here be replaced by p' and q', respectively.

We conclude that ρ_A can be considered maximally nonclassical two-qubit states in terms of the largest REE for a given value of the negativity assuming $N \in (0, N_2)$ or, effectively, for $N \in (N_0, N_2)$ for $N_0 \approx 0.2$. Because ρ_A can be generated from $|\psi_p\rangle$ by amplitude damping and from $\sigma_{\rm D}$ by an unbalanced BS, we can consider these two classes of states to be related to the maximally nonclassical single-qubit states in terms of the largest REEP as a function of the NP for $\bar{N} \in (0, N_2)$ or, clearly, for $\bar{N} \in (N_0, N_2)$.

7. Boundary states $\rho_{\rm B}$ by phase damping

Here we show, after Refs. [22,25], how to generate the boundary states ρ_B from $|\psi_p\rangle$, first by transforming it to $|\Psi_{\rm out}(p)\rangle$ and then to $|\Psi_q\rangle$ and, finally, applying phase damping. This method is analogous to generating ρ_A by amplitude damping, which is here replaced by phase damping described the Kraus operators [4]:

$$E_0(\kappa_i) = |0\rangle\langle 0| + \sqrt{1-\kappa_i}|1\rangle\langle 1|, \quad E_1(\kappa_i) = \sqrt{\kappa_i}|1\rangle\langle 1|, \tag{A17}$$

with κ_i being phase-damping coefficients with $i = 1, 2$. Thus, a pure state $|\Psi_q\rangle$ is changed into the mixed state [25]:

$$\begin{aligned}\rho_{\rm PDC}(q, \kappa_1, \kappa_2) = &\left(\tfrac{1}{2} - y\right)|\beta_1\rangle\langle\beta_1| + \left(\tfrac{1}{2} + y\right)|\beta_2\rangle\langle\beta_2| \\ &+\left(q - \tfrac{1}{2}\right)(|\beta_1\rangle\langle\beta_2| + |\beta_2\rangle\langle\beta_1|),\end{aligned} \tag{A18}$$

given in the Bell-state basis, where $|\beta_{1,2}\rangle = |\Psi_\mp\rangle = (|10\rangle \mp |01\rangle)/\sqrt{2}$ and $y = \sqrt{q(1-q)(1-\kappa_1)(1-\kappa_2)}$. If we assume the input state $|\psi_{p=1}\rangle = |1\rangle$, which corresponds to setting $q = 1/2$, then $\rho_{\rm PDC}$ becomes the following Bell-diagonal state:

$$\begin{aligned}\rho_{\rm B}(\kappa_1, \kappa_2) &= \rho_{\rm PDC}\left(\tfrac{1}{2}, \kappa_1, \kappa_2\right) \\ &= \lambda_-|\beta_1\rangle\langle\beta_1| + \lambda_+|\beta_2\rangle\langle\beta_2|,\end{aligned} \tag{A19}$$

where $\lambda_\pm = [1 \pm \sqrt{(1-\kappa_1)(1-\kappa_2)}]/2$. The states $\rho_{\rm B}(\kappa_1, \kappa_2)$ for $\kappa_i \in [0, 1]$ are examples of the boundary states labeled B in Figs. 2 and 4.

Indeed, the states ρ_B can be interpreted as the maximally nonclassical two-qubit states in terms of the largest negativity for a given value of the REE [24,25]. Since ρ_B can be generated from $|1\rangle$, we have produced experimentally the maximally nonclassical single-qubit states in terms of the largest (generalized) NP as a function of the (generalized) REEP in almost the entire range [0,1], as shown in Fig. 4(c).

[1] C. H. Bennett and G. Brassard, Quantum cryptography: Public key distribution and coin tossing, Theor. Comput. Sci. **560**, 7 (2014).

[2] P. W. Shor and J. Preskill, Simple proof of security of the BB84 quantum key distribution protocol, Phys. Rev. Lett. **85**, 441 (2000).

[3] A. K. Ekert, Quantum cryptography based on Bell's theorem, Phys. Rev. Lett. **67**, 661 (1991).

[4] M. A. Nielsen and I. L. Chuang, *Quantum Computation and Quantum Information*, 10th anniversary ed. (Cambridge University Press, Cambridge, 2010).

[5] E. J. S. Fonseca, C. H. Monken, and S. Pádua, Measurement of the de Broglie wavelength of a multiphoton wave packet, Phys. Rev. Lett. **82**, 2868 (1999).

[6] J. Jacobson, G. Björk, I. Chuang, and Y. Yamamoto, Photonic de Broglie waves, Phys. Rev. Lett. **74**, 4835 (1995).

[7] R. J. Glauber, *Quantum Theory of Optical Coherence: Selected Papers and Lectures* (Wiley, Weinheim, Germany, 2007).

[8] M. Hillery, Nonclassical distance in quantum optics, Phys. Rev. A **35**, 725 (1987).

[9] C. T. Lee, Measure of the nonclassicality of nonclassical states, Phys. Rev. A **44**, R2775 (1991).

[10] N. Lütkenhaus and S. M. Barnett, Nonclassical effects in phase space, Phys. Rev. A **51**, 3340 (1995).

[11] J. K. Asbóth, J. Calsamiglia, and H. Ritsch, Computable measure of nonclassicality for light, Phys. Rev. Lett. **94**, 173602 (2005).

[12] A. Miranowicz, K. Bartkiewicz, A. Pathak, J. Peřina, Y.-N. Chen, and F. Nori, Statistical mixtures of states can be more quantum than their superpositions: Comparison of nonclassicality measures for single-qubit states, Phys. Rev. A **91**, 042309 (2015).

[13] A. Kenfack and K. Życzkowski, Negativity of the Wigner function as an indicator of non-classicality, J. Opt. B **6**, 396 (2004).

[14] A. Mari, K. Kieling, B. M. Nielsen, E. S. Polzik, and J. Eisert, Directly estimating nonclassicality, Phys. Rev. Lett. **106**, 010403 (2011).

[15] A. Miranowicz, J. Kadlec, Bartkiewicz, A. Černoch, Y.-N. Chen, K. Lemr, and F. Nori, Quantifying nonclassicality of vacuum-one-photon superpositions via potentials of Bell nonlocality, quantum steering, and entanglement, arXiv:2309.12930.

[16] A. Miranowicz, M. Bartkowiak, X. Wang, Y.-X. Liu, and F. Nori, Testing nonclassicality in multimode fields: A unified derivation of classical inequalities, Phys. Rev. A **82**, 013824 (2010).

[17] J. Kadlec, K. Bartkiewicz, A. Černoch, K. Lemr, and A. Miranowicz, Experimental hierarchy of the nonclassicality of single-qubit states via potentials for entanglement, steering, and Bell nonlocality, Opt. Express **32**, 2333 (2024).

[18] W. K. Wootters, Entanglement of formation of an arbitrary state of two qubits, Phys. Rev. Lett. **80**, 2245 (1998).

[19] G. Vidal and R. F. Werner, Computable measure of entanglement, Phys. Rev. A **65**, 032314 (2002).

[20] R. Horodecki, P. Horodecki, M. Horodecki, and K. Horodecki, Quantum entanglement, Rev. Mod. Phys. **81**, 865 (2009).

[21] V. Vedral, M. B. Plenio, M. A. Rippin, and P. L. Knight, Quantifying entanglement, Phys. Rev. Lett. **78**, 2275 (1997).

[22] A. Miranowicz, K. Bartkiewicz, N. Lambert, Y.-N. Chen, and F. Nori, Increasing relative nonclassicality quantified by standard entanglement potentials by dissipation and unbalanced beam splitting, Phys. Rev. A **92**, 062314 (2015).

[23] A. Miranowicz and A. Grudka, Ordering two-qubit states with concurrence and negativity, Phys. Rev. A **70**, 032326 (2004).

[24] A. Miranowicz and A. Grudka, A comparative study of relative entropy of entanglement, concurrence and negativity, J. Opt. B **6**, 542 (2004).

[25] B. Horst, K. Bartkiewicz, and A. Miranowicz, Two-qubit mixed states more entangled than pure states: Comparison of the relative entropy of entanglement for a given nonlocality, Phys. Rev. A **87**, 042108 (2013).

[26] K. Życzkowski, P. Horodecki, A. Sanpera, and M. Lewenstein, Volume of the set of separable states, Phys. Rev. A **58**, 883 (1998).

[27] K. Życzkowski, Volume of the set of separable states. II, Phys. Rev. A **60**, 3496 (1999).

[28] C. K. Hong, Z. Y. Ou, and L. Mandel, Measurement of subpicosecond time intervals between two photons by interference, Phys. Rev. Lett. **59**, 2044 (1987).

[29] M. Ježek, J. Fiurášek, and Z. Hradil, Quantum inference of states and processes, Phys. Rev. A **68**, 012305 (2003).

[30] E. Halenková, A. Černoch, K. Lemr, J. Soubusta, and S. Drusová, Experimental implementation of the multifunctional compact two-photon state analyzer, Appl. Opt. **51**, 474 (2012).

[31] D. F. V. James, P. G. Kwiat, W. J. Munro, and A. G. White, Measurement of qubits, Phys. Rev. A **64**, 052312 (2001).

[32] J. Altepeter, E. Jeffrey, and P. Kwiat, Photonic state tomography, Adv. At. Mol. Opt. Phys. **52**, 105 (2005).

[33] A. Miranowicz, K. Bartkiewicz, J. Peřina, Jr., M. Koashi, N. Imoto, and F. Nori, Optimal two-qubit tomography based on local and global measurements: Maximal robustness against errors as described by condition numbers, Phys. Rev. A **90**, 062123 (2014).

[34] K. Bartkiewicz, A. Černoch, K. Lemr, and A. Miranowicz, Priority choice experimental two-qubit tomography: Measuring one by one all elements of density matrices, Sci. Rep. **6**, 19610 (2016).

[35] E. Knill, R. Laflamme, and G. J. Milburn, A scheme for efficient quantum computation with linear optic, Nature (London) **409**, 46 (2001).

[36] K. Lemr, A. Černoch, J. Soubusta, and J. Fiurášek, Experimental preparation of two-photon Knill-Laflamme-Milburn states, Phys. Rev. A **81**, 012321 (2010).

[37] See Supplemental Material at http://link.aps.org/supplemental/10.1103/PhysRevA.110.023720 for raw and processed experimental data along with the processing scripts.

[38] K. Jiráková, A. Černoch, K. Lemr, K. Bartkiewicz, and A. Miranowicz, Experimental hierarchy and optimal robustness of quantum correlations of two-qubit states with controllable white noise, Phys. Rev. A **104**, 062436 (2021).

[39] S. Abo, J. Soubusta, K. Jiráková, K. Bartkiewicz, A. Černoch, K. Lemr, and A. Miranowicz, Experimental hierarchy of two-qubit quantum correlations without state tomography, Sci. Rep. **13**, 8564 (2023).

[40] M. A. Nielsen, Conditions for a class of entanglement transformations, Phys. Rev. Lett. **83**, 436 (1999).

[41] K. Bartkiewicz, B. Horst, K. Lemr, and A. Miranowicz, Entanglement estimation from Bell inequality violation, Phys. Rev. A **88**, 052105 (2013).